Engineering Fracture Mechanics 323 (2025) 111199

Contents lists available at ScienceDirect

Engineering Fracture Mechanics

journal homepage: www.elsevier.com/locate/engfracmech

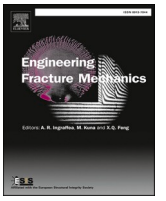

Tensile behaviour and residual stress characterisation of bio-inspired laser weld joints☆

Manish Kumar [a,*], Vladimir Luzin [b,c], Filippo Berto [d], Paolo Ferro [e,*], Enrico Salvati [a,*]

[a] Dipartimento Politecnico di Ingegneria e Architettura, University of Udine, Via delle Scienze, 206, 33100 Udine, Italy
[b] Australian Centre for Neutron Scattering (ACNS) - The Australian Nuclear Science and Technology Organisation (ANSTO), New Illawarra Road, Lucas Heights, NSW 2234 Sydney, Australia
[c] School of Engineering, The University of Newcastle, Callaghan, NSW 2308, Australia
[d] Department of Chemical Engineering Materials Environment, University of Rome "La Sapienza", Via Eudossiana, 18, 00184 Roma, Italy
[e] University of Padova, Department of Engineering and Management, Stradella S. Nicola, Vicenza, Italy

ARTICLE INFO

Keywords:
Bio-inspired weld patterns
Residual stresses
Heat affected zone
Uniaxial tensile tests, Mechanical behaviour
Elastoplastic FE simulations

ABSTRACT

Inspired by principles observed in nature, bio-inspired welding patterns can be designed to emulate the load-bearing capacity and resilience of natural interlocking structures. This study introduces bio-inspired interlocking weld patterns as alternatives to traditional linear welds, aiming to modify residual stress distribution and examine the effects on static tensile properties. Quasi-static mechanical properties and residual stress of two bio-inspired patterns were assessed and compared to linear welds and base material. Neutron diffraction was used to evaluate residual stresses, while mechanical testing and Finite Element Method (FEM) were employed to evaluate the stress–strain response of the analysed materials. This model generated numerical values for the heat-affected zone (HAZ) properties, enabling the creation of an empirical relationship to predict HAZ extent based on weld geometry. Experimental validation showed strong agreement with the model, and a parametric analysis investigated how weld shape and dimensions influence the joint performance. While the study did not reveal a significant reduction in residual stress magnitudes for the studied geometric configurations, it provided valuable insights into the ways welding patterns can influence stress distribution. Tensile properties were notably affected by the bio-inspired patterns, showing a significant increase in yield strength. An interpretation of these results is also provided.

1. Introduction

Welding is one of the most used metal joining processes, given its rapidness and efficiency in rigidly bonding similar and dissimilar metallic materials. In fusion-based welding processes, metals are melted for a short time in the joining region to accelerate their mechanical interdiffusion and produce a continuous mechanical part. These melted metals are recrystallised during the resolidification which also affects the neighbouring region. The neighbouring region is generally the weakest part of a joint, and it is

☆ This article is part of a special issue entitled: 'CP2024' published in Engineering Fracture Mechanics.

* Corresponding authors.
E-mail addresses: manish.kumar@uniud.it (M. Kumar), paolo.ferro@unipd.it (P. Ferro), enrico.salvati@uniud.it (E. Salvati).

https://doi.org/10.1016/j.engfracmech.2025.111199
Received 11 February 2025; Received in revised form 28 March 2025; Accepted 29 April 2025
Available online 4 May 2025

Nomenclature

a	Amplitude of the bio-inspired pattern weld
b	Half period of the bio-inspired pattern weld
T_{EHAZ}^{Pat}	Thickness of EHAZ of bio-inspired pattern weld
T_{HAZ}^{Lin}	Thickness of HAZ of linear weld
xx	Transverse direction
yy	Longitudinal direction
zz	Normal direction
γ-Fe	Face-centred cubic iron
σ_{xx}	Transverse stress component
σ_{yy}	Longitudinal stress component
$\sigma_{y'y'}$	Longitudinal stress component with reference to a local coordinate system
σ_{xy}	Shear stress component
ANSTO	Australian Nuclear Science and Technology Organisation
EHAZ	Effective Heat-Affected Zone
FEM	Finite Element Method
HAZ	Heat-Affected Zone

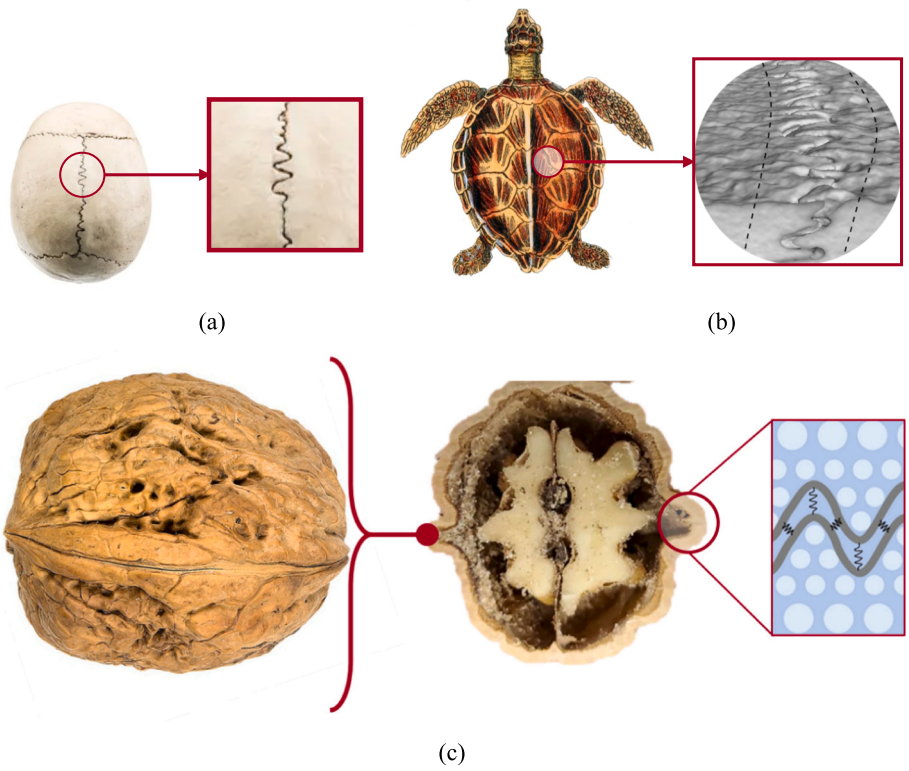

Fig. 1. The interlocking joint patterns found in nature (a) adult human skull suture, (b) tortoise shell (c) walnut shell (re adapted from [39]).

known as Heat Affected Zone (HAZ). Different thermal expansions and contractions of the fusion zone and HAZ constrain the solidification of molten metal, leading to thermal gradients and subsequent strain mismatch. Residual stresses arise in the fusion zone and HAZ as a consequence of thermal history and mismatch of strain. These residual stresses can reach magnitudes as high as the yield stress [13,37]. Many approaches were proposed to decrease these residual stresses through various post-weld heat treatments for different materials [14,24,33]. The post-weld heat treatments proved their beneficial effect [7,29]. Nevertheless, the complete removal of residual stress across the large-scale components appears to be utopistic. This presence of residual stresses in HAZ of welded parts makes it a critical area even after post-weld treatments, especially when of a tensile nature, leading to premature failures in various

Table 1
Chemical composition of the AISI 304 (w%).

C	Mn	P	S	Si	Cr	Ni	Other
0.07	2.00	0.045	0.015	1.00	17.0–20.0	8.0–11.0	≤ 0.11

Table 2
Water jet cutting parameters used to create the butt-weld surface.

Parameter	Value
Pressure (bar)	1500
Abrasive flow rate (kg/min)	0.34
Abrasive size	80 mesh
Abrasive index	0.9
Speed (mm/min)	600

conditions such as fatigue failures [6,8,9,10,32], hot cracking [5,15,16,25,28] and many more. The scientific community is working continuously to reduce the HAZ or residual stress due to welding by improving the existing conventional welding methods or inventing new non-conventional welding techniques. Amongst non-conventional welding, friction stir welding [22,26,31,35], Electron beam welding [23,38], Hybrid metal and extrusion bonding [34] and laser welding [1,2,27]demonstrated and improved joint strength.

Although current efforts are focused on the improvement of welding methods or post-welding treatments, the geometrical path of the welding seam is yet to be explored. Most of the welded joints in applications have linear patterns but, one may wonder what would happen to the weld's structural performance if the path is no longer linear. In nature, most of the joints have interlocking patterns such as adult human skull sutures, tortoise shell and walnut shell (readapted from [39]) as shown in Fig. 1.

Based on these natural designs, the present paper proposes to replace the classic linear weld pattern with a bio-inspired interlocking pattern. By adopting this newly conceived concept, a significant alteration of the mechanical properties of the joint is expected, as well as the distribution of residual stresses. Recently, numerical simulations performed by some of the authors of the present manuscript [12] shed some insightful light on the possibility of altering the residual stress distribution and possibly tuning it. Motivated by these encouraging findings, the authors attempted to experimentally investigate the quasi-static performance and residual stress characteristics of the newly conceived welding configuration.

As far as the quasi-static structural performance of the joints is concerned, three different welding path scenarios were examined. Alongside, the parent material was characterised for comparison. The laser welding technique was employed to produce these welds for an AISI 304 stainless steel. Alongside the tensile properties of the welded joints, the residual stresses induced by the weld patterns were also experimentally evaluated by neutron diffraction.

Additionally, a numerical methodology was developed to evaluate the static strength of the welded joint. Several numerical approaches to model welded joints were summarised in the literature [21]. In the last decade, new approaches emerged to improve the accuracy and applicability, such as coupled thermo-mechanical analysis [3], virtual element for weld bead [30] and many more. In the current study, a methodology is developed based on the Finite Element Method (FEM) due to its simplicity and robustness. This method is inspired by the work done by Krejsa et al. [20], Krejsa et al. [18] and Krejsa et al. [19] in which weld and HAZ are considered as different materials. This concept is easy to implement and can model the various shapes of welds. Eventually, the developed methodology can simulate the elastoplastic behaviour of both the linear and the bio-inspired welds. The major contributions of the present study are given below:

- Uniaxial tensile experiments were performed for AISI 304 with linear and bio-inspired weld patterns.
- Residual stresses were evaluated for various weld patterns using neutron diffraction in all directions.
- A numerical framework is proposed to simulate the bio-inspired weld patterns to compute their mechanical behaviour.
- The effect of size and shape of bio-inspired welds on joint strength was investigated by parametric analysis.

The article is divided into four sections, the motivation and inspiration of the problem are mentioned in **Section 1**. The material specifications and specimen preparation for various weld patterns along with experimental procedures are explained in **Section 2**. The numerical simulation framework for the bio-inspired weld patterns is also presented in **Section 2**. Experimental and numerical findings for uniaxial tests and residual stress measurements are reported and discussed in **Section 3**. Numerical parametric analysis is also presented in **Section 3**. The summary of the present study is mentioned in **Section 4**.

2. Material and methods

The above-mentioned concept of using a bio-inspired weld pattern to change the joint properties is evaluated both experimentally and numerically. An austenitic stainless steel AISI 304 was chosen to perform these assessments. The chemical composition of the steel was obtained through a UV Master Foundry© spectrometer and reported in Table 1. The sample preparation details, along with experimental and numerical procedures are described in the following subsections.

Table 3
Laser welding parameters used to produce the butt welds.

Parameter	Value
Torch Speed (*mm*/min)	600
Spot (*mm*)	0.27
Clamping	Table with rules
Laser power (*W*)	600
Focus (*mm*)	+3
Gas	Nitrogen
Gas flow rate (*l*/min)	20

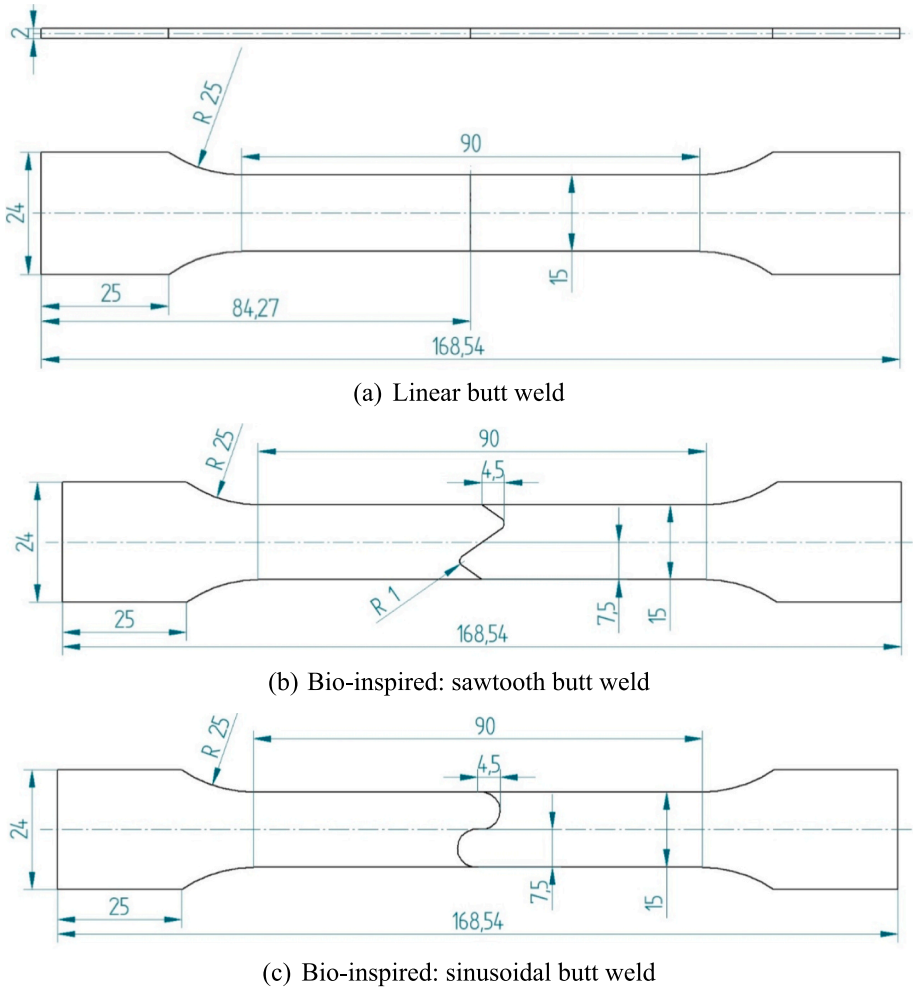

Fig. 2. Uniaxial tensile specimen with (a) linear (b) bio-inspired: sawtooth (c) bio-inspired: sinusoidal butt weld patterns. (Dimensions in millimetres).

2.1. Sample preparation

A sheet of 298 × 179 × 2 *mm* was taken to prepare the specimens. The dimensions of the specimen to acquire the tensile strength of metallic material's weld through destructive test were taken from UNI EN ISO 4136:2012 standard [36]. Water jet cutting was used to obtain the desired butt-welding surface i.e., linear and bio-inspired patterns. The use of a high-pressure and high-speed jet of water in this process made it fast and precise for small pieces without introducing additional deformation while limiting the heat induced in the workpiece during cutting. Water jet cutting parameters used to make the weld surfaces are tabulated in Table 2. The produced clean and smooth finished surfaces were welded by laser beam welding. In this welding technique, a laser beam is focused on the component to heat the material. The melting temperature is rapidly achieved in a small region, which produces a deep, narrow, and precise joint. The welding parameters used to produce the welds are given in Table 3. Eventually, specimens of 15 *mm* width and 90 *mm* gauge length

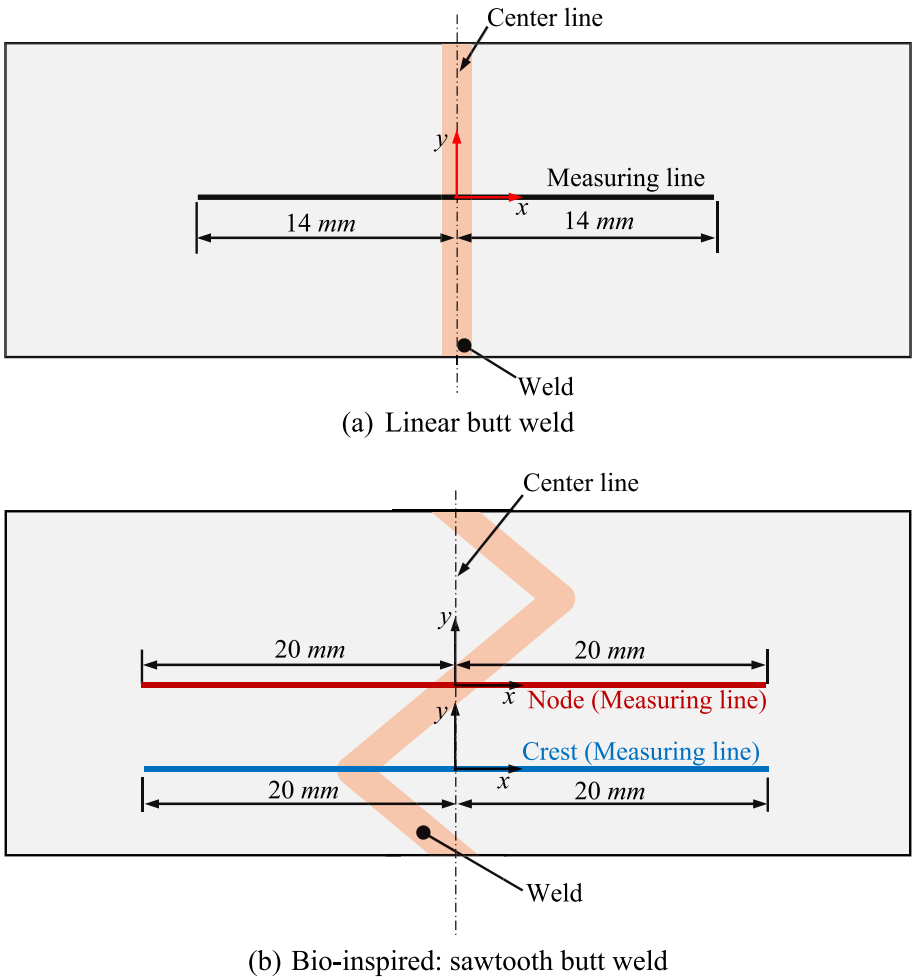

Fig. 3. An illustration of the considered locations for the measurement of residual stresses by neutron diffraction (a) linear (b) bio-inspired: sawtooth butt weld patterns.

were cut from the parent plates, again using water jet cutting. The produced specimens for linear butt weld, bio-inspired patterns i.e. sawtooth butt weld, and sinusoidal butt weld, along with dimensions are shown in Fig. 2. respectively.

2.2. Experimental procedures

Uniaxial tensile tests were performed with the prepared specimens using a 30-ton Instron© model:4486 machine in displacement control configuration. An extensometer of 25 *mm* was used to measure the longitudinal strain in the specimen. The obtained data from these experiments were analysed and processed to attain the fundamental mechanical properties and stress–strain behaviour, which is reported in the next section.

As far as the welding residual stresses are concerned, neutron diffraction was used for their evaluation in two conditions: linear weld and bio-inspired sawtooth weld. Such evaluations were performed at the KOWARI beamline of the Australian Nuclear Science and Technology Organisation (ANSTO) [17]. A monochromatic neutron beam having a wavelength of 1.53 Å was employed to probe the material in a nominal gauge volume of $0.7 \times 0.7 \times 0.7\ mm^3$. The evaluation of residual stress was conducted through the exploitation of the γ-Fe (311) reflection plane. Both the bio-inspired weld patterns showed similar responses thus, neutron diffraction was performed only on the sawtooth weld pattern.

The three normal strains were measured in the normal (zz), longitudinal (yy) and transverse (xx) directions, according to the illustration in Fig. 3, to be able to reconstruct two in-plane stress components, (σ_{xx}) and (σ_{yy}), while through-thickness stresses were neglected given the relatively small thickness of the welded plates, so the plane stress condition is applicable. The shear residual stress (σ_{xy}) was also measured for the bio-inspired weld to explore its localized asymmetric nature. The evaluations were performed over a spatial linear extent of 14 *mm* and 20 *mm* on either side of the centre line for linear and bio-inspired: sawtooth butt weld, respectively as shown by the measuring lines in Fig. 3. In the case of bio-inspired sawtooth weld, the evaluations were done at two distinct locations

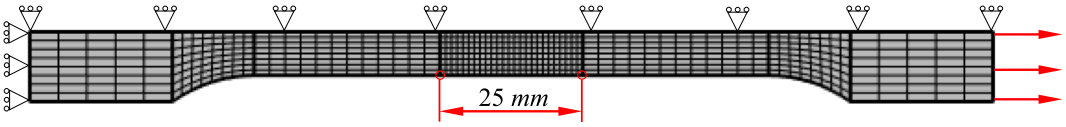

Fig. 4. Computational model used to perform the uniaxial tensile simulation for parent material where red circles represent the extensometer (of 25 *mm* length) location. (For interpretation of the references to colour in this figure legend, the reader is referred to the web version of this article.)

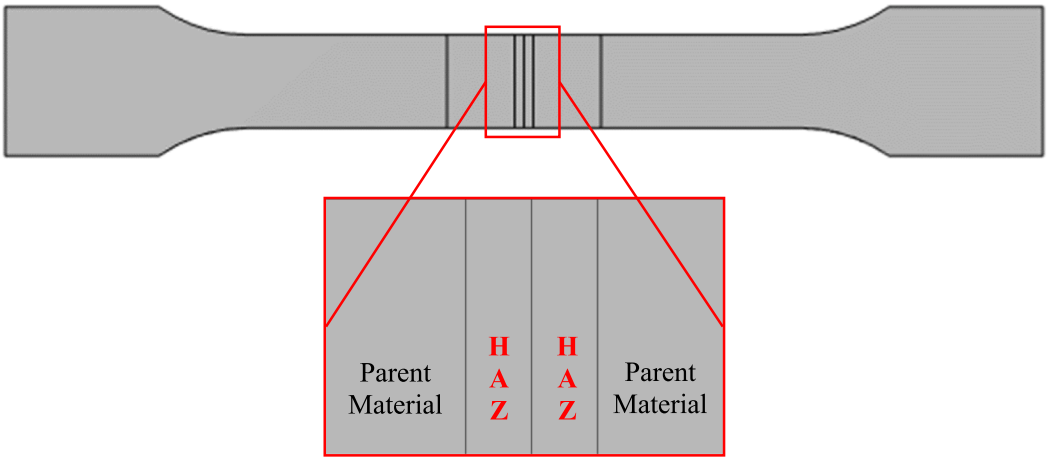

Fig. 5. An illustration of subdomains: parent material and HAZ to model the weld.

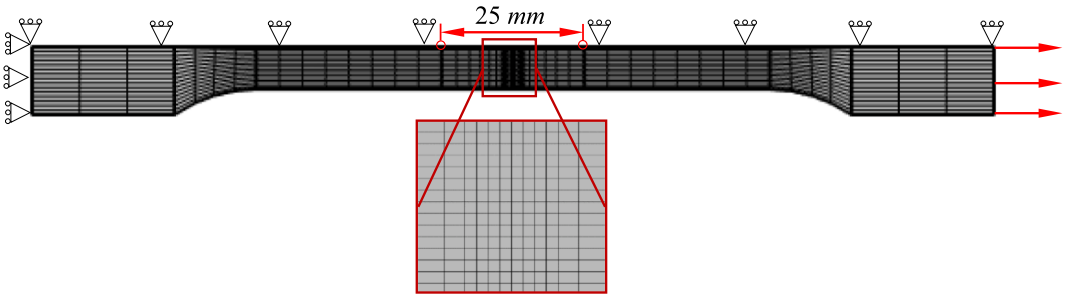

Fig. 6. Computational model prepared to perform the uniaxial tensile simulation for linear weld.

named: Node and Crest. Node refers to the straight part of the weld while Crest is for the curved part as presented in Fig. 3(b).

2.3. Numerical modelling

Elastoplastic numerical simulations were performed to shed light on the origin of the characteristic stress–strain behaviour of the bio-inspired weld configurations. The commercially available finite element software COMSOL [4] was used for these simulations. At first, a simulation for the parent material was performed to assess the framework followed by the simulations for weld configurations. The fundamental material properties along with the plastic behaviour obtained from the uniaxial tensile experiments were used as input to create the computational models for these simulations. The von Mises yield criterion was implemented in the simulations along with the associated flow rule and isotropic hardening. The isotropic hardening was modelled with interpolation of provided plastic stress–strain data. The strain was evaluated at the location of the extensometer to be consistent with experiments, whereas the force was obtained through the integration of the stress component in the loading direction and divided with the cross-sectional area to obtain the stress. For the parent material simulation, a half model with 600 hexahedral elements was used in which the element size was $1 \times 1 \times 1$ *mm* in the gauge length. The computational model for parent material simulation along with boundary conditions is shown in Fig. 4. The location of the extensometer used to compute the strain is also illustrated in Fig. 4.

To extend the established computational model for welded specimens, the HAZ is modelled with different material properties than the parent material. In this way, the model appears as a composite of two materials i.e. parent material and HAZ material. The geometry of the specimen is divided into subdomains as presented in Fig. 5 and the corresponding material properties are assigned to

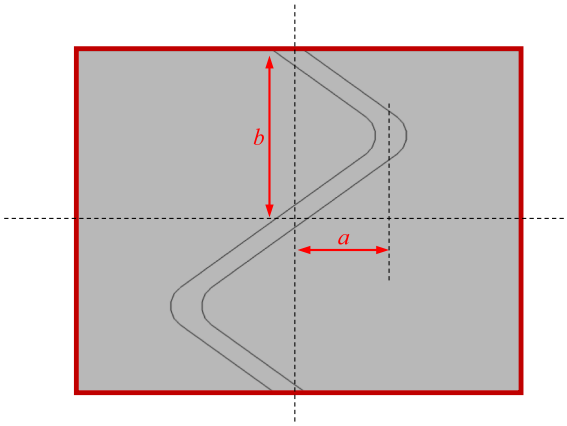

Fig. 7. Dimensional features of the bio-inspired weld pattern to find its EHAZ thickness.

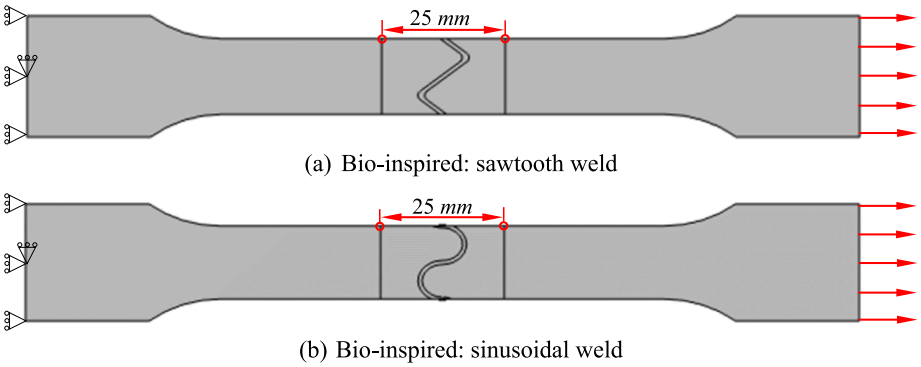

Fig. 8. Computational model used to perform the uniaxial tensile simulation for (a) bio-inspired: sawtooth and (b) bio-inspired: sinusoidal weld patterns.

these domains. The thickness of the HAZ is determined using the Vicker hardness results [11]. The hardness increased significantly near the weld, which presented the HAZ for the weld. The obtained value for the thickness of HAZ for the linear weld is 1.5 *mm* on either side of the weld. In order to perform the simulation via this approach, material properties of HAZ were required which were found numerically. An iterative computational approach was employed in which tentative material properties for HAZ were assigned as input to the model. The computed stress–strain behaviour was compared with the experimental linear weld case. Based on this comparison, appropriate changes were made to iteratively tune HAZ material properties. This process continued until a satisfactory agreement between the computed results and experimental observations was achieved. Analogously to the parent material simulation, one of the symmetries of the geometrical model and loads was exploited to prepare the computational model of the linear weld as shown in Fig. 6, consisting of 750 hexahedral elements with element size in the heat affected zone of $0.5 \times 0.5 \times 1$ *mm*.

The established framework and numerically obtained HAZ material properties were taken as the basis to perform the simulations for the bio-inspired weld patterns. However, acquiring the HAZ thickness for these weld patterns was not straightforward because there was no notable change in Vicker hardness as reported by Ferro et al. [11]. Moreover, these measurements also depend on the location of the weld. As shown in Fig. 3, the bio-inspired weld has different regions such as crest and node that have different characteristics. Thus, for these simulations, instead of exact HAZ thickness an effective HAZ thickness (denoted as EHAZ in the article) needs to be assessed using an alternative approach. For this purpose, an empirical relation depending on the geometry of the weld pattern is proposed:

$$T_{EHAZ}^{Pat} = \left(1 - \frac{1.223\ a}{b}\right) T_{HAZ}^{Lin} \qquad for\ a/b \leqslant 0.8 \tag{1}$$

where, T_{EHAZ}^{Pat} and T_{HAZ}^{Lin} is the thickness of EHAZ of bio-inspired pattern weld and HAZ of linear weld respectively, a and b are the feature dimensions of weld pattern as presented in Fig. 7, a is the amplitude and b is the half period. Differently from the previously analysed weld geometries, no symmetries could be exploited this time. Both the computational models for bio-inspired weld patterns, sawtooth and sinusoidal, are shown in Fig. 8. Upon conducting a mesh convergence study, the element size in the effective heat affected zone was considered as $0.15 \times 0.15 \times 1$ *mm* for both cases resulting in a total of 1694 and 3708 hexahedral elements for sawtooth and

Table 4
Material properties of the parent material and various weld patterns.

Property	Parent material	Linear weld	Sawtooth weld	Sinusoidal weld
Young's Modulus	183 GPa	183 GPa	183 GPa	183 GPa
Poisson Ratio	0.27	0.27	0.27	0.27
Yield Tensile Strength	333 MPa	294 MPa	316 MPa	317 MPa
Ultimate Tensile Strength	670 MPa	671 MPa	672 MPa	679 MPa

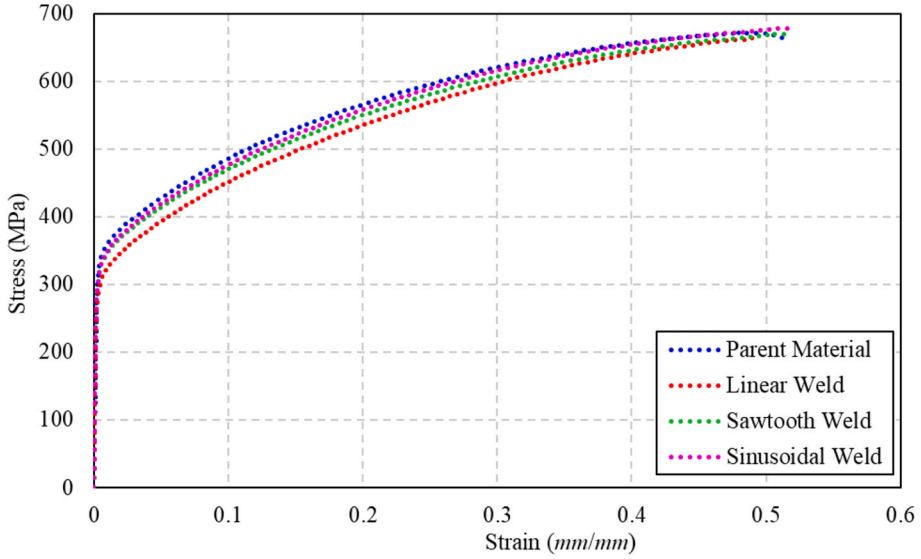

Fig. 9. Comparison of the stress–strain behaviour of the parent material and weld patterns.

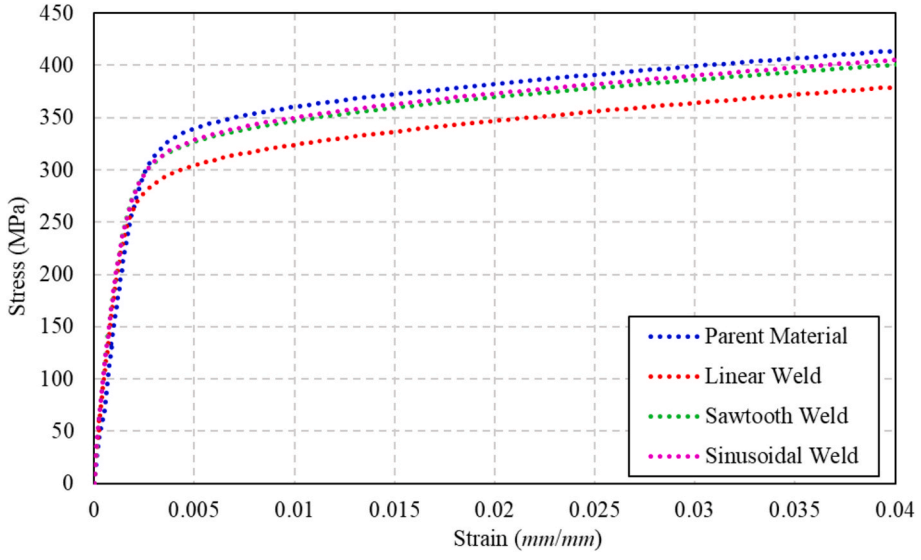

Fig. 10. Enlarged view of the yielding region of the stress–strain behaviour of the parent material and weld patterns.

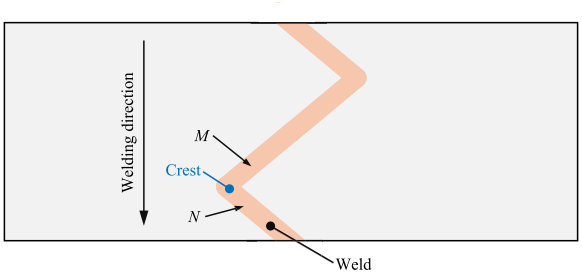

Fig. 11. Illustration of pre-heating and post-heating in the crest region of the bio-inspired weld.

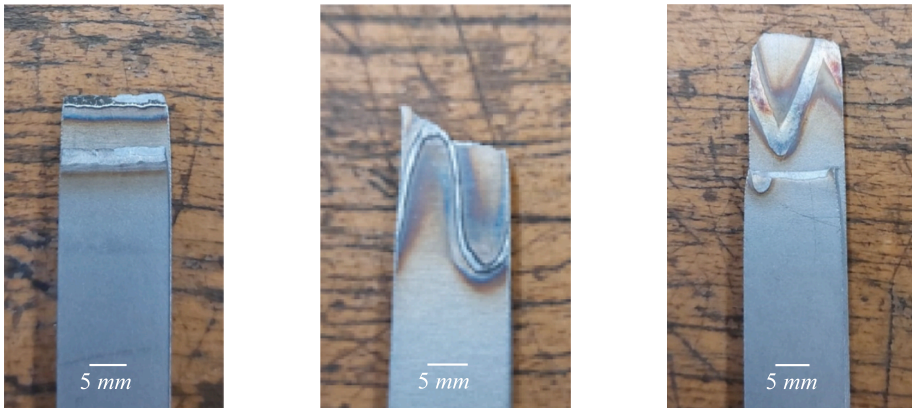

Fig. 12. Raptured surface of the various butt weld patterns: (a) linear, (b) bio-inspired: sawtooth (c) bio-inspired: sinusoidal.

sinusoidal pattern, respectively. The stress and strain were computed in a similar way as mentioned in the previous paragraphs. A parametric analysis was performed by varying the geometrical dimensions of the weld, which is discussed in the next section.

3. Results and discussions

In this section, the experimental and numerical results for the uniaxial tensile specimens with various weld configurations are presented. The carried-out numerical parametric study is also reported in this section. Experimentally evaluated residual stresses for linear weld and bio-inspired weld are compared. These findings are discussed in detail in the following subsections.

3.1. Uniaxial tensile experiments

The fundamental mechanical properties obtained from the uniaxial tensile experiments for parent material and all weld patterns (linear, bio-inspired) are tabulated in Table 4. The obtained data from these experiments showed the significant effects on the yielding region. Thus, the focus of this study was on the yielding region. The tests were repeated on multiple specimens (two specimens for the parent material and three specimens for each welding configuration) to have more reliable results. The average stress–strain behaviour from these different tests is presented in Fig. 9 for the parent material and all the weld patterns. The stress values from different experiments were interpolated for a particular strain data from one experiment and a non-biased summation average was taken to obtain the average stress–strain behaviour. The standard deviation of all the experiments in the interested region is 0.2–1.1 MPa. The stress–strain behaviours from these experiments showed similar behaviour for the rapture as displayed in Fig. 9 while in the region of yielding the observations were remarkably interesting as shown by its enlarged view in Fig. 10. The obtained results showed a significant decrease in the yield strength of the linear butt weld as compared to the parent material, which was expected. However, for the bio-inspired patterns (sawtooth and sinusoidal), there was an increase of 7–8 % in the yield strength as compared to the linear weld. In the bio-inspired weld path, the laser beam had to cover more distance than the linear path at the same speed, which altered the thermal strain distributions. This alteration would be high near the crest region of the joint. As illustrated in Fig. 11, when the beam reached point *M* near the start of the crest it pre-heated the area near the end of the crest (Point *N*) while when the beam was at point *N* it post-heated the region near the start of the crest (Point *M*). The effect of this pre-heating and post-heating is more severe as compared to the linear weld. It happens because of time taken to cover that distance is more, which affects the joint failure location and residual stresses

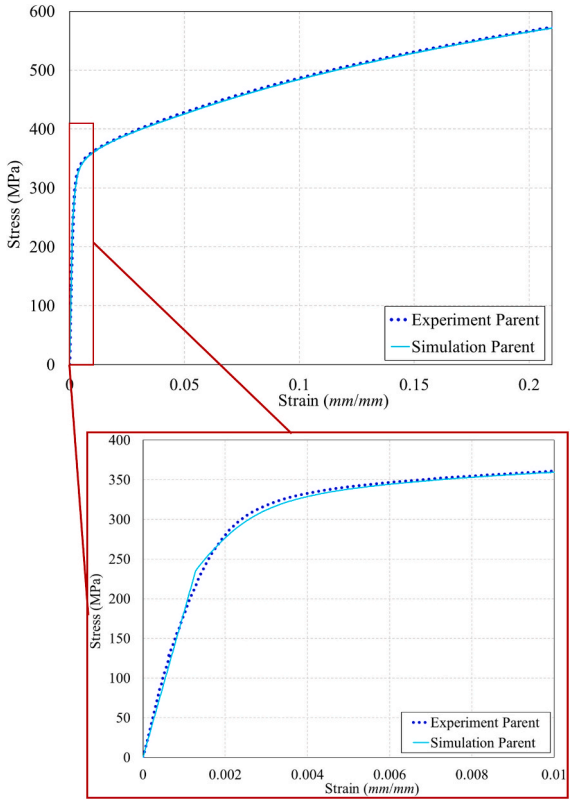

Fig. 13. Comparison of the numerically computed stress–strain behaviour of the parent material with experimental observations.

as discussed in the following paragraphs. Eventually, all these phenomena have a positive effect on the yield strength of the bio-inspired joint.

The location for the rapture was different for these welds as shown in Fig. 12, the rapture surface for linear weld is near the joint while for the bio-inspired weld, rapture surfaces are close to the curvature of the pattern. A plausible reason for this difference is the HAZ, which is straight in the case of linear weld and is perpendicular to the loading direction. This configuration makes the entire failure surface run along the HAZ, leading to a lower yielding strength. On another end, for the bio-inspired weld pattern, HAZ follows the weld, and it is not perpendicular to the loading direction which restricts the development of the entire failure surface in HAZ. Thus, the obtained failure surface is hybrid (HAZ + parent material), as can be seen in Fig. 12. This hybrid failure surface demonstrates a diffuse yielding, taking place simultaneously at the weld HAZ and the border to the unaffected parent material.

3.2. Numerical simulations of uniaxial tensile experiments

At first, a simulation for the parent material was performed to test the framework. The computational model shown in Fig. 4, and the material data from Table 4 and Fig. 9 were used for this simulation. As expected, the predicted stress–strain behaviour is in very good agreement with the experimental observations, as shown in Fig. 13, given that it was calibrated by these quantitative experimental outcomes. The enlarged view of the yielding region is also presented in Fig. 13. Therefore, this framework can be extended for the welded specimens, as explained in the following subsections.

The proposed approach of modelling HAZ as a different material which is explained in Subsection 2.3 was used for the computational model shown in Fig. 6. The material properties for the HAZ were computed numerically in an iterative way, which resulted in the yield strength equal to 182 MPa while the estimated complete stress–strain behaviour is presented in Fig. 14. The stress–strain behaviour of the linear weld joint for the uniaxial tensile model was evaluated using these HAZ material properties. The obtained numerical results are compared with experimental results in Fig. 14 that are in good agreement as expected. The evaluated material behaviour is also presented in an enlarged view of the yielding region in Fig. 14. From this comparison, it is verified that these HAZ properties can be treated as material properties and used as input for bio-inspired weld patterns.

Numerically acquired material properties of HAZ, which are presented in Fig. 14 were used as EHAZ's material properties as input for the already described computational models (Fig. 8) for bio-inspired welds. The thickness of EHAZ was obtained with the help of Eq. (1) for both bio-inspired welds: sawtooth and sinusoidal. The results from both simulations were compared with the experimental findings and are reported in Fig. 15. The numerical results are found in good agreement with experiments, and an increase in the yield strength for the bio-inspired welds can be noticed as compared to the linear case. The comparison of stress–strain behaviour in the

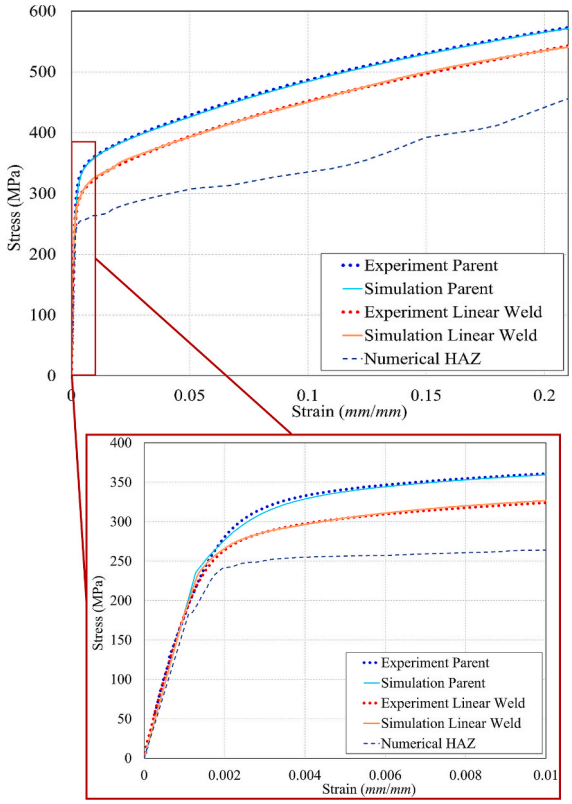

Fig. 14. Comparison of numerically obtained stress–strain behaviour of the linear weld with experimental results and parent material's behaviour.

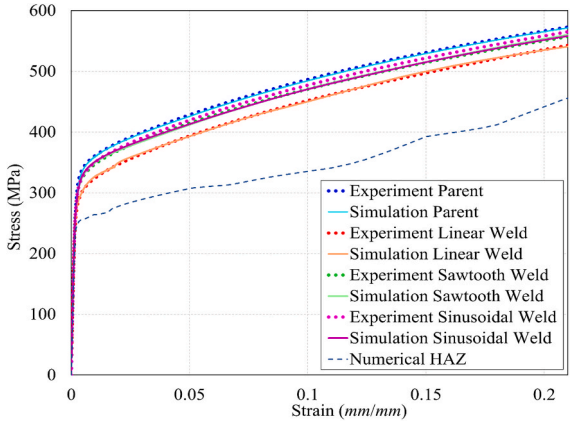

Fig. 15. Comparison of numerically computed stress–strain behaviour of all the weld patterns with experimental results.

yielding region is shown by an enlarged plot in Fig. 16. These comparisons validate the presented numerical approach to model various weld patterns. Hence, the presented computation model is capable of predicting the material response for these types of weld patterns and can be used further to optimise the shape of the weld patterns as described with a parametric study in the following paragraph.

3.2.1. Parametric study

Both the bio-inspired weld patterns showed similar responses thus, the parametric study was performed only on the sinusoidal weld pattern. This parametric study was performed with the validated model of the bio-inspired sinusoidal weld model. The geometric dimension of the weld, a (amplitude) was varied as 3 *mm*, 3.75 *mm*, 4.5 *mm*, and 5.25 *mm*. The EHAZ of the weld pattern was calculated by Eq. (1) and the prepared model for this study is presented in Fig. 17. The same approach as explained in the previous subsections was implemented to compute the stresses and strains in these models. The parametric results are compared with parent material (both

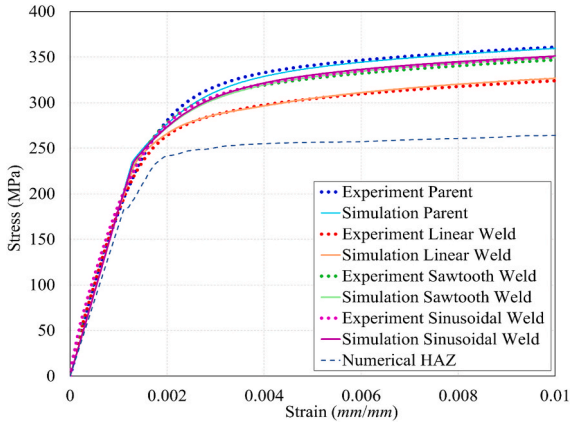

Fig. 16. Enlarged view of the yielding region of numerically computed stress–strain behaviour of all the weld patterns and experimental results.

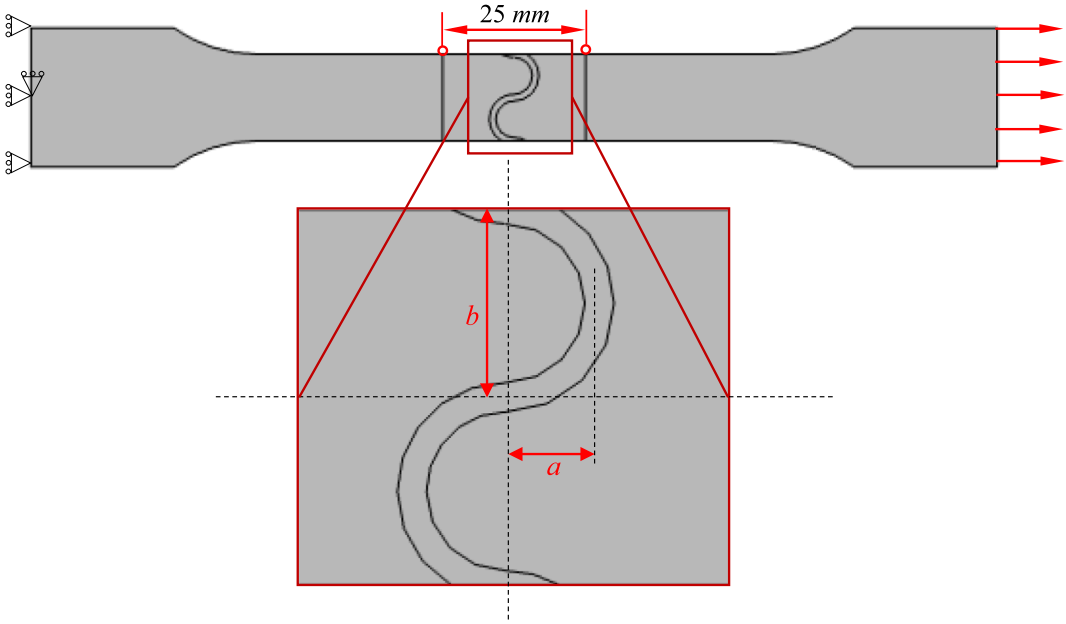

Fig. 17. Computational model prepared for bio-inspired weld patterns with different values of *a*.

experimental and simulation) in Fig. 18. The enlarged plot of the stress–strain behaviour in the yielding region is also displayed in Fig. 18. This parametric study concludes that with the increase in amplitude, the bio-inspired weld pattern has higher yield strength and comes closer to the parent material.

3.3. Welding residual stresses

The evaluated residual stresses by neutron diffraction for the bio-inspired sawtooth weld clearly have a higher magnitude and wider extent as compared to the linear weld. For the interpretation of these evaluations, the coordinate systems are defined as presented in Fig. 19(a). The intersection of the centre line and measuring line is assigned as an origin (‘0′) for all the measurements. The left side of the defined origin is denoted as negative while the right side is positive. These evaluations were done with the interval of 1 *mm* on the measuring line and obtained distributions of residual stresses for all the probed spatially resolved positions are presented in Fig. 19. The evaluated residual stress in the longitudinal direction is shown in Fig. 19(b). The transverse and shear stresses are significantly lower than the longitudinal component as can be seen in Fig. 19(c) and (d), as typically happens in welds when transversal constraints are absent. In fact, for straight path welding, the parent metal self-constrains the expansions and contractions of the weld bead in the longitudinal direction during its heating and cooling phase while, in the transverse direction the Fusion Zone and HAZ are free to expand and contract without any constraint, thus reducing the resulting residual stresses to a minimum in transverse direction.

A completely different thermal history characterizes sawtooth welding. In fact, due to the curvature of the welding path the

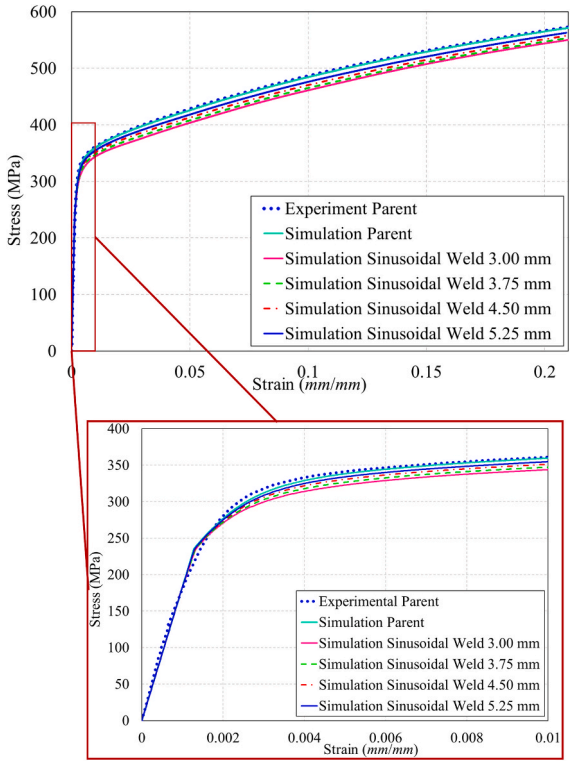

Fig. 18. Numerically computed stress–strain behaviour of bio-inspired weld patterns with different values of *a*.

material undergoes a greater pre-heating and post-heating as highlighted in Ferro et al. [12]. More pre-heating and post-heating result in a slightly wider weld bead and larger volume of the molten zone than that induced by a rectilinear weld for the same welding process parameters. A larger volume of the molten zone consequent greater contraction effect during the cooling phase explains the higher values of the longitudinal residual stresses measured in the sawtooth welding compared to those measured in the standard welding as shown in Fig. 19(b). The peak magnitude of the longitudinal residual stress at the node and crest locations of the sawtooth weld is quite the same. However, these values are dependent on the geometric parameters of the welding path and pioneering works in the literature [12] demonstrate that they can be calibrated simply by varying the geometric parameters of the welding path.

The longitudinal residual stresses for sawtooth weld have a wider extent than linear weld because of the extra weld coverage in the transverse dimension as shown in Fig. 19(a). The residual stress shows a symmetrical extent for the linear weld and node location of the sawtooth weld, whereas, for the crest of the sawtooth weld it is asymmetrical which is discussed in more detail in the next subsection.

Finally, the absence of the shear component in the "node" or "crest" locations demonstrates the fact that the stress distribution is not really sensitive to the local weld path (scale of ~ 1 mm) but rather congruent to the overall extent of the weld and HAZ regions (scale of ~ 20 mm), thus, the principal stress axes are related to the overall sample geometry, but not to the local direction of the weld path.

3.3.1. Remarks on the extent of longitudinal residual stresses

In order to gain insights regarding the extent of the longitudinal residual stresses, local coordinate systems are defined as presented in Fig. 20(a), i.e., *x'-y'*. The intersection of the weld seam centre and measuring line is assigned as an origin ('0') for the linear weld and node location of sawtooth weld patterns, whereas, for the crest of sawtooth weld, the origin is defined at the intersection of the measuring line and weld centre. The left side of the welded region is denoted as negative, while the right side is positive. The peak of residual stresses for all the cases lies near the origin with these local coordinate systems as shown in Fig. 20(b). The extent of longitudinal residual stress for linear weld and node location for bio-inspired weld is symmetric, but for the crest location, it has a wider extent on the internal side of the crest than on the external one, which can be observed distinctly in Fig. 20(b). The plausible reason for the asymmetric extent is the thermal history of bio-inspired weld. It leads to a higher accumulation of heat in the internal area of the crest as compared to its outside area, which reduces the thermal gradient in the internal area. A similar type of residual stress distribution was obtained numerically by some of the authors of the present paper and published in Ferro et al. [12]. It is important to highlight that, although the peak residual stress magnitudes slightly increase when the sawtooth pattern is considered, as compared with the linear weld, there exists an apparent reduction of the region extent experiencing tensile residual stress at the outer area of the crest profile. Again, this is attributed to the rapid heat flux that the outer regions are subjected to.

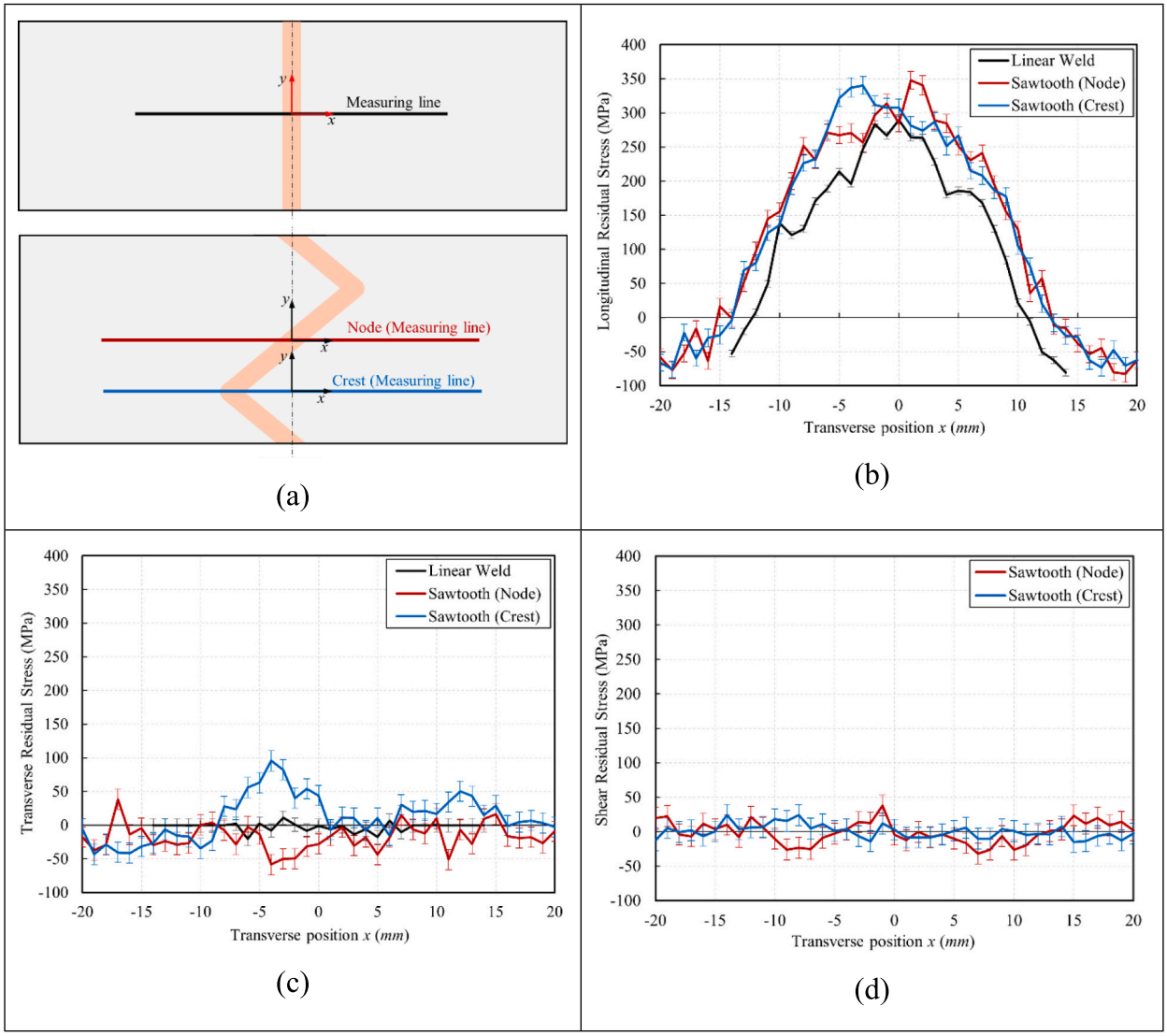

Fig. 19. Residual stress distributions obtained through neutron diffraction (a) Reference frames for linear and sawtooth butt weld patterns, respectively; (b) Longitudinal residual stress (σ_{yy}); (c) Transverse residual stress (σ_{xx}); (d) Shear residual stress (σ_{xy}).

4. Conclusions

In the current work, experimental and numerical investigations are carried out to shed light on the static properties of bio-inspired welding patterns along with their tensile behaviour and residual stress.

The main findings and observations from this research are as follows:

- The yield strength of bio-inspired weld patterns (sawtooth and sinusoidal) was found to be 7–8 % higher as compared to the linear weld. Such a difference was attributed to the different thermal histories induced by the studied paths.
- Longitudinal residual stresses show higher magnitudes and wider extents for sawtooth weld as compared to the linear weld that is in consent with a wider area of weld/HAZ regions and more heat input introduced by welding.
- The internal side of the crest location of bio-inspired weld has a wider extent of longitudinal residual stresses as compared to the external side. The external side is narrower than the linear weld configuration. This is experimental evidence of the capability of this joint to limit tensile residual stresses in regions where necessary in practical engineering applications.
- The material properties of HAZ were indirectly evaluated through a FEM-based numerical approach.
- The proposed numerical framework can be used to optimise the yield properties of the bio-inspired weld as demonstrated in a parametric study presented in this article.

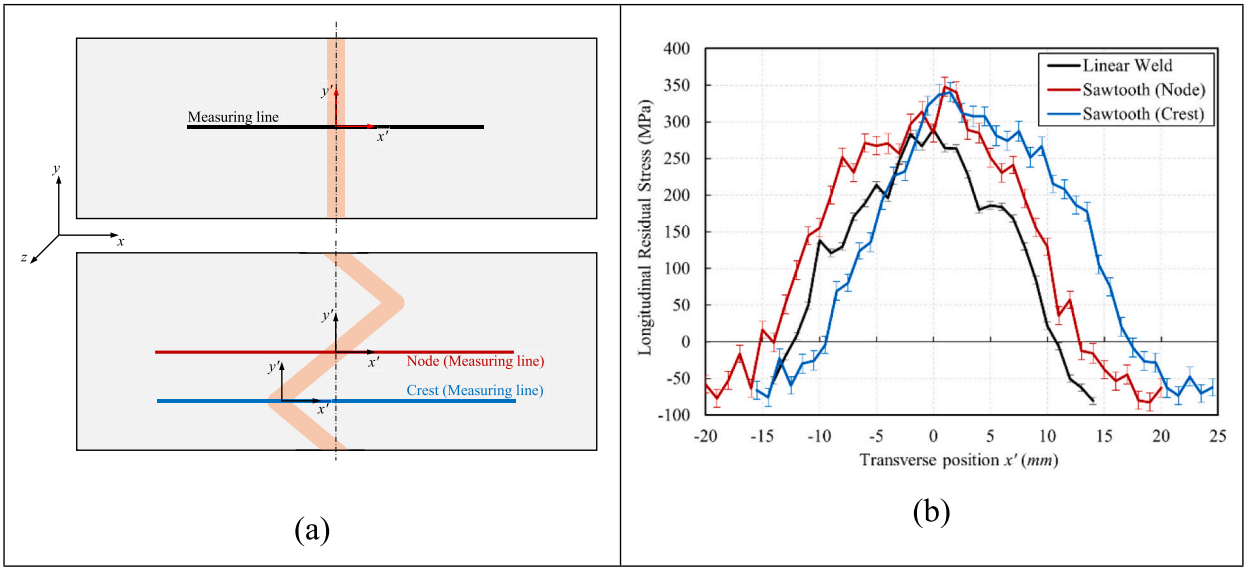

Fig. 20. Longitudinal residual stress distributions obtained through neutron diffraction (a) Local reference frames for linear and sawtooth butt weld patterns, respectively; (b) Longitudinal residual stress ($\sigma_{y'y'}$).

The results shown in this paper provided fundamental experimental and numerical insights into the parameters affecting the static properties of the manufactured welds. The proposed bio-inspired weld patterns are anticipated to affect the joint properties under fatigue conditions, which will be the focus of future work.

Funding support

This work has been supported by the following projects.

"NutShell – NUmerical modelling and opTimisation of SHELL Structures Against Fracture and Fatigue with Experimental Validations" funded by the MUR Progetti di Ricerca di Rilevante Interesse Nazionale (PRIN) Bando 2022, Italy – NextGenerationEU – PNRR M4.C2.1.1 – PRIN 2022 – Codice 20229BM9EL – CUP G53D23001140006.

"CONCERTO – Multiscale modelling/ characterisation and fabrication of nanocomposite ceramics with improved toughness'' funded by the MUR Progetti di Ricerca di Rilevante Interesse Nazionale (PRIN) Bando 2020, Italy – grant 2020BN5ZW9.

"A Phase Field Framework to Predict Fatigue Cracking Incorporating Residual Stresses and Hydrogen Effects" funded by the MIUR Piano Nazionale di Ripresa e Resilienza (PNRR) Bando 2022- CUP G23C22002710007.

CRediT authorship contribution statement

Manish Kumar: Writing – original draft, Validation, Software, Methodology, Conceptualization. **Vladimir Luzin:** Writing – review & editing, Investigation, Conceptualization. **Filippo Berto:** Methodology, Conceptualization. **Paolo Ferro:** Writing – review & editing, Investigation, Conceptualization. **Enrico Salvati:** Writing – review & editing, Validation, Supervision, Resources, Project administration, Methodology, Conceptualization.

Declaration of competing interest

The authors declare that they have no known competing financial interests or personal relationships that could have appeared to influence the work reported in this paper.

Data availability

Data will be made available on request.

References

[1] Arfaoui L, Samet A, Znaidi A. Identification of the anisotropic behavior of the laser welded Interstitial Free steel HC260Y subjected to uniaxial tensile tests. *Fracture and Structural Integrity* 2022;16(61):282–93.

[2] Auwal S, Ramesh S, Yusof F, Manladan SM. A review on laser beam welding of copper alloys. *Int J Adv Manuf Technol* 2018;96:475–90.

[3] Chiumenti M, Cervera M, de Saracibar CA, Dialami N. Numerical modeling of friction stir welding processes. *Comput Methods Appl Mech Engng* 2013;254:353–69.
[4] COMSOL Multiphysics®. COMSOL AB, Stockholm, Sweden.
[5] Coniglio N, Cross C. Effect of weld travel speed on solidification cracking behavior. Part 1: weld metal characteristics. *Int J Adv Manuf Technol* 2020;107:5011–23.
[6] Delkhosh E, Khurshid M, Barsoum I, Barsoum Z. Fracture mechanics and fatigue life assessment of box-shaped welded structures: FEM analysis and parametric design. *Weld World* 2020;64:1535–51.
[7] Dong P, Song S, Zhang J. Analysis of residual stress relief mechanisms in post-weld heat treatment. *Int J Press Vessel Pip* 2014;122:6–14.
[8] Ferro P. The local strain energy density approach applied to pre-stressed components subjected to cyclic load. *Fatigue Fract Engng Mater Struct* 2014;37(11):1268–80.
[9] Ferro P, Berto F. Quantification of the influence of residual stresses on fatigue strength of Al-alloy welded joints by means of the local strain energy density approach. *Strength Mater* 2016;48:426–36.
[10] Ferro P, Berto F, James N. Asymptotic residual stress distribution induced by multipass welding processes. *Int J Fatigue* 2017;101:421–9.
[11] Ferro P, Dabalà M, Meneghello R, Savio G, Berto F, Salvati E. Microstructure, distortion and residual stress investigation in a bio-inspired welding pattern. *Procedia Struct Integrity* 2024;66:287–95.
[12] Ferro P, Tang K, Berto F, Salvati E. Tuning residual stresses in welded structures by exploiting bio-inspired suture interfaces. *Fatigue Fract Engng Mater Struct* 2024.
[13] Hemmesi K, Farajian M, Boin M. Numerical studies of welding residual stresses in tubular joints and experimental validations by means of x-ray and neutron diffraction analysis. *Mater Des* 2017;126:339–50.
[14] Huang B, Liu J, Zhang S, Chen Q, Chen L. Effect of post-weld heat treatment on the residual stress and deformation of 20/0Cr18Ni9 dissimilar metal welded joint by experiments and simulations. *J Mater Res Technol* 2020;9(3):6186–200.
[15] Jindal S, Chhibber R, Mehta N. Issues in welding of HSLA steels. *Adv Mat Res* 2012;365:44–9.
[16] Jing H, Chao F, Jin L, Jing W. Study on molten pool flow and hot cracking of narrow gap laser welding of 316LN stainless steel for fusion reactor. *Opt Laser Technol* 2025;181:111633.
[17] Kirstein O, Luzin V, Garbe U. The strain-scanning diffractometer Kowari. *Neutron News* 2009;20(4):34–6.
[18] Krejsa M, Brozovsky J, Mikolasek D, Parenica P, Flodr J, Materna A, et al. Numerical modeling of steel fillet welded joint. *Adv Engng Softw* 2018;117:59–69.
[19] Krejsa M, Brozovsky J, Mikolasek D, Parenica P, Koubova L. *Static behavior of the weld in the joint of the steel support element using experiment and numerical modeling*. Paper presented at the IOP Conference Series: Earth and Environmental Science. 2018.
[20] Krejsa M, Brozovsky J, Mikolasek D, Parenica P, Koubova L, Materna A. Numerical modeling of fillet and butt welds in steel structural elements with verification using experiment. *Procedia Engng* 2017;190:318–25.
[21] Lindgren LE. Numerical modelling of welding. *Comput Methods Appl Mech Engng* 2006;195(48–49):6710–36.
[22] Liu F, Hovanski Y, Miles M, Sorensen C, Nelson T. A review of friction stir welding of steels: tool, material flow, microstructure, and properties. *J Mater Sci Technol* 2018;34(1):39–57.
[23] Liu X, Dong Q, Wang P, Chen H. Review of electron beam welding technology in space environment. *Optik* 2021;225:165720.
[24] Luo Y, Gu W, Peng W, Jin Q, Qin Q, Yi C. A study on microstructure, residual stresses and stress corrosion cracking of repair welding on 304 stainless steel: Part i-effects of heat input. *Materials* 2020;13(10):2416.
[25] Maurya AK, Pandey C, Chhibber R. Dissimilar welding of duplex stainless steel with Ni alloys: A review. *Int J Press Vessel Pip* 2021;192:104439.
[26] Mishra A, Dasgupta A. Optimization of the mechanical property of friction stir welded heat treatable aluminum alloy by using bio-inspired artificial intelligence algorithms. *Fracture and Structural Integrity* 2022;16(62):448–59.
[27] Nabavi SF, Farshidianfar A, Dalir H. A comprehensive review on recent laser beam welding process: geometrical, metallurgical, and mechanical characteristic modeling. *Int J Adv Manuf Technol* 2023;129(11):4781–828.
[28] Norouzian M, Elahi MA, Plapper P. A review: Suppression of the solidification cracks in the laser welding process by controlling the grain structure and chemical compositions. *J Adv Joining Proc* 2023;7:100139.
[29] Olabi A, Hashmi M. The effect of post-weld heat-treatment on mechanical-properties and residual-stresses mapping in welded structural steel. *J Mater Process Technol* 1995;55(2):117–22.
[30] Romanin L, Ferro P, Berto F. A simplified non-linear numerical method for the assessment of welding induced deformations. *Mar Struct* 2021;78:102982.
[31] Salih OS, Ou H, Sun W, McCartney D. A review of friction stir welding of aluminium matrix composites. *Mater Des* 2015;86:61–71.
[32] Salvati E. Evaluating fatigue onset in metallic materials: Problem, current focus and future perspectives. *Int J Fatigue* 2024;108487.
[33] Suominen L, Khurshid M, Parantainen J. Residual stresses in welded components following post-weld treatment methods. *Procedia Engng* 2013;66:181–91.
[34] Tognan A, Sandnes L, Totis G, Sortino M, Berto F, Grong Ø, et al. Evaluation and origin of residual stress in hybrid metal and extrusion bonding and comparison with friction stir welding. *Int J Mech Sci* 2022;218:107089.
[35] Tognan A, Sheshi N, Vaglio E, Luzin V, Hattingh D, Salvati E. Multimodal experimental and numerical evaluation of Residual Stress in AA6082-T6 Friction Stir Welding pipe girths. *J Mater Process Technol* 2025;335:118665.
[36] UNI EN ISO 4136:2012 (2012). Destructive tests on welds in metallic materials - Transverse tensile test. Geneva: International Organization for Standardization (ISO).
[37] van den Berg N, Xin H, Veljkovic M. Effects of residual stresses on fatigue crack propagation of an orthotropic steel bridge deck. *Mater Des* 2021;198:109294.
[38] Węglowski MS, Błacha S, Phillips A. Electron beam welding–techniques and trends–review. *Vacuum* 2016;130:72–92.
[39] Xu P, Wang L, Liu J, Yue Y, Fan Y. Effects of geometrical characteristics of suture on fracture resistance of walnut shell. *J Bionic Engng* 2023;20(6):2732–41.